Biosourced adsorbent prepared with rice husk part 1: A complete understanding of the structure of materials, the major role of mineral impurities for metal extraction

Baptiste Russo, Jérémy Causse, Cyrielle Rey, Joseph Lautru, Diane Rebiscoul, André Ayral

Biosourced adsorbent prepared with rice husk part 1: a complete understanding of the structure of materials, the major role of mineral impurities for metal extraction.

Baptiste RUSSO [a *], *Jérémy CAUSSE* [a], *Cyrielle REY* [a], *Joseph LAUTRU* [a], *Diane REBISCOUL* [a], *André AYRAL* [b]

[a] CEA, ICSM – UMR 5257 CEA-CNRS-UM-ENSCM, 30207 Bagnols-sur-Cèze Cedex, France

[b] Institut Européen des Membranes, IEM – UMR 5635, ENSAM, CNRS, Univ Montpellier, Montpellier, France

*Corresponding author: E-mail address: russo.baptiste@gmail.com (B. RUSSO)

Biosourced adsorbent prepared with rice husk part 1: a complete understanding of the structure of materials, the major role of mineral impurities for metal extraction.

Abstract

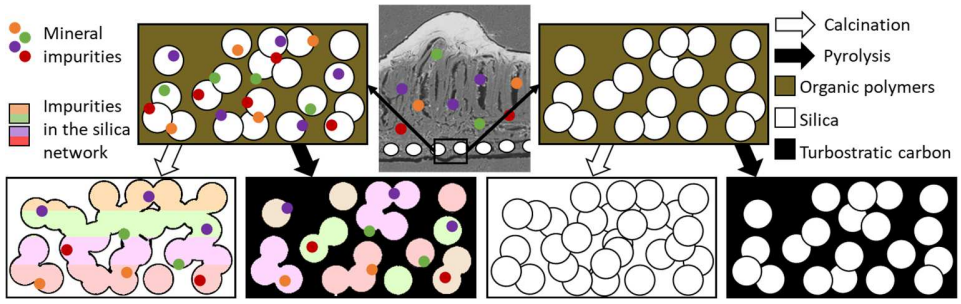

Rice husk is a global agricultural co-product and is already the subject of several studies, notably for wastewater treatment. Rice husk is composed of 3 types of components: amorphous silica, organic biopolymers and others (salts, oxides...). Depending on the treatment, rice husk becomes either a carbon-free material or a mixed carbon/silica biochar. In this paper, a thorough characterisation of rice husk was carried out by SEM, TEM, TGA, XRF, XRD, XPS, FTIR, SAXS, SANS, NMR and N_2 adsorption-desorption. The results show that silica can be present as dense silica or silica nanoparticles and that native organic matter can be converted to turbostratic carbon. This carbon "drowns" the silica nanoparticles and prevents them from sintering. Particular attention is paid to impurities which play a crucial role in several properties. They are present in different forms, such as $CaCO_3$, KCl or Al_2O_3 or in the silica lattice. They can be removed, but if retained, they induce sintering and crystallisation of the silica nanoparticles, resulting in a decrease in specific surface area from 330 $m^2.g^{-1}$ to 15 $m^2.g^{-1}$. Moreover, the sorption efficiency of the materials is strongly dependent on the presence of impurities since the extraction rate drops drastically from 99 % to less than 0.5 % when the impurities are removed. The maximum capacity reached for nickel is 11.7 $mg.g^{-1}$.

Keywords

Rice husk, rice husk ash, silica, biochar, nanostructure.

1. Introduction

In the face of increasing difficulties in providing clean water to the population, many current studies are trying to develop solutions to remove contaminants from polluted water[1-3]. To join this effort, more and more studies are being conducted to promote the circular economy and the use of biomass for wastewater treatment, especially the use of biochars[4,5]. Rice husk (RH) is the inedible part of the grain that is removed after harvest. Currently, rice husk is widely available and a large amount is waiting to be valorised. In France alone, which accounts for only 0.1 wt‰ of the world rice production[6], there is an annual yield of 16 500 t of RH. It is mostly used as a fuel for thermal power generation but other uses can be found inthe building materials or steel production sectors[7]. Since the last decade, a large number of studies have invested the potential of RH as a sorbent for water depollution. Indeed, the presence of a large amount of natural silica (≈ 20 wt%), cellulose, hemicellulose and lignin in RH allows the preparation of a mixed biochar (carbon/SiO_2) after a simple heat treatment[8]. This material is a potential candidate for removing pollutants from effluents containing both inorganic and organic contaminants. Indeed, several researchers have demonstrated that RH derivatives can be used to remove Cd[9-11], Co[12], Cu[13-16], Hg[17,18], Ni[19,20], Pb[21-24], Zn[25,26], dyes[27-29], pyridine[30] or phenolic compounds[31-33] from wastewater. However, the fine characterisation of its microstructure has not benefited from the same investigation. In particular, the microstructure of the silica and the interaction between carbon and silica are not well described, nor is the nature of the impurities, which are often simply considered as oxides[34,35]. Indeed, even if the nanostructure of silica is discussed in some papers[36-40], its interaction with the carbon phase is rarely mentioned[41] and the crucial importance of impurities is not always linked to the sorption property although some authors have understood their importance[9,16,23,24]. When the microstructure of silica is studied, it is often considered either as nanoparticules or as dense, but never both. According to the researchers, the dense phase is due to the sintering of the silica nanoparticles because of the presence of potassium[38,42,43]. In the present study, another look is taken and it is shown that these two structures can coexist with each other. The entanglement of carbon phase and silica nanoparticles is only mentioned in two articles so far and is not really studied in depth[41,44]. Here, a full understating of the consequences of such an entanglement is brought to light, particularly on the sintering of silica. Finally, little attention is paid in the literature to the impurities present in the raw material. In general, they are considered as oxides, with the exception of very few papers[45,46], and are often removed by an acid treatment[13,18]. In this study, special attention is

given to them because of their crucial role in the removal of metals from wastewater. Furthermore, as this is the first time that French RH is studied for use as a wastewater solution, its full characterisation is necessary to compare it with other RH and to ensure its appropriate use in this field.

2. Methods

2.1. Material used and sample preparation

The batches of raw rice husk (RRH) were provided by the "silos of Tourtoulen" located in the Camargue (Arles, France). As a first step, part of the rice husk was washed on a 1 mm sieve with MilliQ™ water to remove dust. In order to remove mineral impurities, the sieved rice husk was boiled up to 100 °C in a solution of 2 mol.L^{-1} HNO_3 (69.5 %, Carlo-Erba Reagents) for 1 h and washed again with MilliQ™ water until the pH reached that of ultra-pure water[8]. The treated rice husk (TRH) was finally dried at 100 °C in an oven for 12 h.

RRH and TRH samples were heat treated at 700 °C to obtain either raw rice husk ash (RRHA) or treated rice husk ash (TRHA). If the atmosphere used during the heat treatment is oxidising, such as air (RRHA-Air and TRHA-Air), the carbonaceous part is completely removed and the resulting ash is carbon-free. If the atmosphere used is inert, such as argon (RRHA-Ar and TRHA-Ar), a carbonaceous fraction is retained in the materials, which can be called biochars. Heat treatment of the samples was carried out by placing the materials in a cylindrical alumina crucible open on both sides, which is then introduced in a quartz tube. During the heat treatment, the temperature was increased from room temperature to 700 °C with a heating rate of 5 °C.min^{-1}.

2.2. Characterisation

The morphology, microstructure and composition of the materials were characterised by Scanning Electron Microscopy (SEM). An FEI Quanta 200 FEG environmental scanning electron microscope (ESEM) with a field-emission gun coupled to a Bruker Energy-Dispersive X-ray Spectroscopy (EDX) 125 eV XFlash 5010 with a 10 mm^2 detector was used. The accelerating voltage was 5-6 kV. The EDX images were processed with Esprit 1.9.5 software.

Transmission Electron Microscopy (TEM) images were obtained using a Jeol 2100F microscope (200 kV, Cs-corrected condenser, imaging filter, EDX, biprism, 2 CCD cameras)

with one bright field and one dark field detector. The embedded sample was less than 100 nm thick.

Thermogravimetric analyses (TGA) were performed in a Mettler Toledo Stare System under air or argon at atmospheric pressure with a heating rate of 5 °C min^{-1}. Buoyancy effects were corrected by a blank run with an empty alumina crucible.

Ash impurities were characterised by solid state X-Ray Fluorescence spectroscopy (XRF) using a Spectro Xepos and Spectro X-Labpro V5.1 software. These analyses were mainly qualitative but could also be quantitative by preparing beads incorporating the sample using the fused bead technique with 49.75 wt% of lithium tetraborae, 49.75 wt% of lithium metaborate and 0.5 wt% of lithium bromide[47].

Nitrogen adsorption-desorption analyses were performed using a Micromeritics ASAP 2020 instrument. Prior to analysis, all samples were outgassed at 180 °C for 20 h under high vacuum (10^{-5} Pa). Specific surface area S_{BET}, pore volume V_p and pore size distribution were obtained using the Brunauer–Emmett–Teller (BET) method and the Barret–Joyner–Halenda (BJH) model, respectively. If microporosity was suspected in the sample, the t-plot method was applied using the Harkins and Jura equation.

The SAXS analyses were performed in transmission geometry with a molybdenum source, delivering a wavelength of 0.71 Å. Focusing and wavelength selection were achieved using a Xenocs Fox 2D multilayer mirror. Two sets of scatter-free slits were used to collimate the beam into a square shape of 0.8 mm on each side. The SAXS patterns were recorded on a MAR345 2D image plate, which allows simultaneous detection of q scattering vectors ranging from 0.3 to 20 nm^{-1}. The samples were analysed in 2 mm glass capillaries.

The SANS analyses were carried out on PA20 spectrometer of the Orphée reactor at the Léon Brillouin laboratory. This spectrometer was equipped with a multidetector comprising 128 x 128 cells of 5 x 5 mm^2. Several "sample-detector distances/working wavelengths" configurations were used for measurements: 1.5 m/6 Å; 8 m/6 Å; 18 m/6 Å and 18 m/15Å. The samples were placed in a brass sample holder between two quartz discs separated by a 1 mm thick quartz ring. The solid samples were dispersed in pure H_2O.

The molecular structure was analysed using a Perkin Elmer Spectrum 100 FTIR (Fourier Transformed Infrared Red) spectrometer in ATR mode equipped with a DTGS/KBR detector. The samples were placed on a diamond surface. The spectra were recorded from 400 to 4000 cm^{-1} by accumulating 32 scans with a resolution of 2 cm^{-1}. The background spectrum of

each substrate was then subtracted. In the case of solids analyses, the pressure on the punch was adjusted until the spectra stabilised. Baseline adjustments and normalisation were performed using Spectrum software.

The X-Ray diffraction (XRD) measurements were performed on powder samples with a Bruker D8 advance instrument and a Cu Kα (λ = 1.5406 Å) monochromatic source. The powders were disposed on a low background sample holder and the diffractograms were recorded between 10 and 90 ° with a step size of 0.2 ° per minute.

The X-ray photoelectron spectroscopy (XPS) spectra were obtained from an Escalab 250 device with a monochromatic alumina source (Kα = 1486.6 eV). These measurements were performed at the University of Montpellier. The analysed volume is a 400 µm square with a penetration depth of 5 to 10 nm. The baseline was calculated with the Shirley method while the peaks decompositions were performed using Gauss-Lorentz curves on ThermoElectron software.

^{1}H, ^{13}C and ^{29}Si Nuclear Magnetic Resonance (NMR) spectra were collected using a Bruker Avance III 400 MHz spectrometer equipped with a 4 mm 2-channel MAS probe and Topspin 3.2 software. The solid samples were compacted in a 4 mm ZrO_2 rotor and analyses were performed at a rotation frequency of 12 kHz. Spectra were recorded at 400.13 MHz for ^{1}H, 100.61 MHz for ^{13}C and 79.49 for ^{29}Si. Tetramethylsilane was used as a reference for the chemical shifts analyses.

2.3. Extraction test

Extraction tests were realised with a nickel nitrate salt (Merck, purity > 99 %) solubilised in MilliQ™ water to obtain a 2 mmol.L^{-1} nickel solution. For these tests, 100 mg of material were contacted with 10 mL of solution in a 15 mL tube and stirred with a Heidoph Reax 2 at speed 3 for 24 h at room temperature. The mixture was then filtered through a 0.45 µm cellulose acetate Phenex filter and analysed by XRF.

3. Results and discussion

In this section, complete analyses of RRH, TRH and materials derived from them are presented. These include SEM-EDX images and TGA curves for morphology and composition studies, N_2 adsorption-desorption isotherms, TEM pictures and XRD diffractograms for structure studies. Others analyses are also covered but are only available in the supplementary information, such as XRF spectra, SAXS and SANS curves, XPS, NMR and FTIR-ATR data. All of these

analyses provide an in-depth understanding of the structure of rice husk ash, including the nature of the silica, carbon distribution and impurities composition. Finally, extraction tests that highlight the necessary presence of impurities for the material to be effective are presented.

3.1. Starting husks: RRH and TRH

The overall morphology and composition of RRH are shown in the images obtained by SEM and EDX characterisation (Figure 1). RRH presents a well-organised distribution of bumps on its outer part and a smooth inner part (Figure 1 (a)). Both areas are mainly silica but there is also a carbon-rich area in-between where organic biopolymers are concentrated (Figure 1 (b & c)), which is a well-known repartition[48].

To further investigate the morphology of silica, thin foils were prepared by FIB in the outer and inner parts. The white bar in the cross section corresponds to the location of the thin foil prepared by FIB, α and β symbols are related to the orientation of the obtained sample. These images clearly show that the outer layer is a dense silica while the inner silica layer appears to be mainly composed of aggregated silica nanoparticles (Figure 2 (d)).

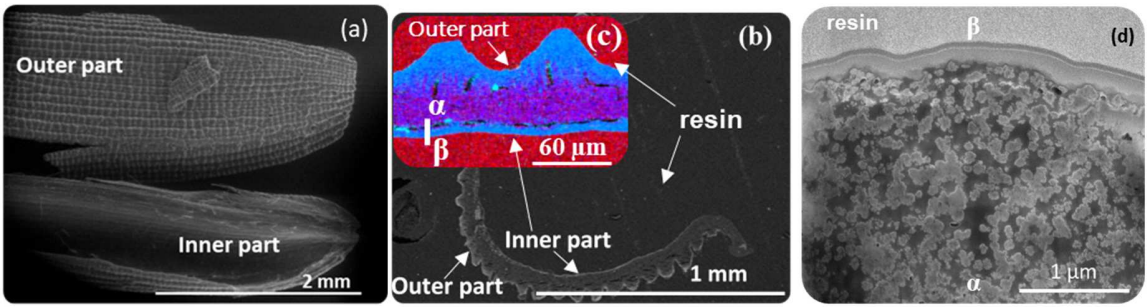

Figure 1. (a) SEM images presenting a global view of RRH, (b) cross section, and (c) associated EDX cartography (carbon in red and silicium in blue) presenting the location of the thin foil and (d) TEM image of the thin foil.

In order to determine the composition of each type of material, RRH and TRH were heat treated under air or argon and the mass loss was monitored by TGA measurements. The TGA curves are presented on Figure 2. Under air (Figure 2.a), 85 wt% of the initial masses of RRH and TRH are degraded by combustion up to about 450 °C for RRH and 600 °C for TRH, these temperatures are consistent with observations made by previous authors[8,49,50] and correspond to the loss of organic compounds such as cellulose, hemicellulose and lignin[51]. The remaining 15 wt% obtained at 1000 °C are minerals. For RRH, this mineral part is composed of about 90 wt% of silica and 10 wt% of mineral impurities such as aluminium, potassium, calcium, manganese

and iron in various forms identified by XRF (S.I. 1). For TRH, the mineral part is only silica as the impurities were removed by hot acidic treatment of RH. During pyrolysis (Figure 2.b), 40 wt% of the initial mass is retained, with the main degradation ending at 350 °C. Again, the observations are consistent with those made by previous authors[8,49,50,52]. Knowing that 15 wt% of the initial mass of RRH are mineral compounds, this means that 25 wt% of the initial weight are carbonaceous compounds. Under argon, RRHA-Ar and TRHA-Ar consist of approximately 60 wt% of carbon and 40 wt% of silica. A slight difference in temperature is observed, resulting in a higher starting degradation temperature for TRH under both atmospheres and a higher ending degradation temperature under air. These differences could be induced by the removal of alkaline earth mineral species that normally catalyse the decomposition of organic compounds[53].

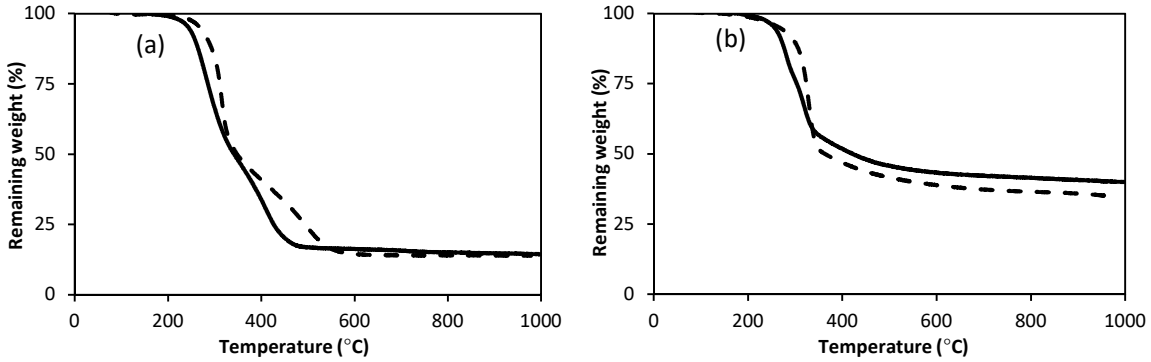

Figure 2. TGA curves for RRH (straight line) and TRH (dotted line) under air (a) or argon (b) atmosphere with a heating rate of 5 °C.min^{-1}.

All these results show that the main change due to the acid treatment is the removal of all impurities of the husk that can no longer catalyse the decomposition of organic compounds anymore. The overall composition and behaviour of this RH is in agreement with other RH in the world.

3.2. Ash obtained under oxidative atmosphere: RRHA-Air and TRHA-Air

The morphologies of RRHA-Air and TRHA-Air were investigated by SEM. As illustrated by the images and EDX mapping presented in Figure 3, the initial morphology of the samples is preserved after the heat treatment but with an overall shrinkage probably due to the decomposition of the organic compounds. Furthermore, while the impurities are retained during combustion in the case of RRHA-Air and can therefore be found in the ash (S.I. 2), none of these impurities are detected by EDX in the TRHA-Air. No carbon was found in either

samples (S.I. 3). The white bar in the cross section corresponds to the location of the thin foil prepared by FIB and analysed by TEM, α and β symbols describe the orientation of the resulting sample (Figure 5).

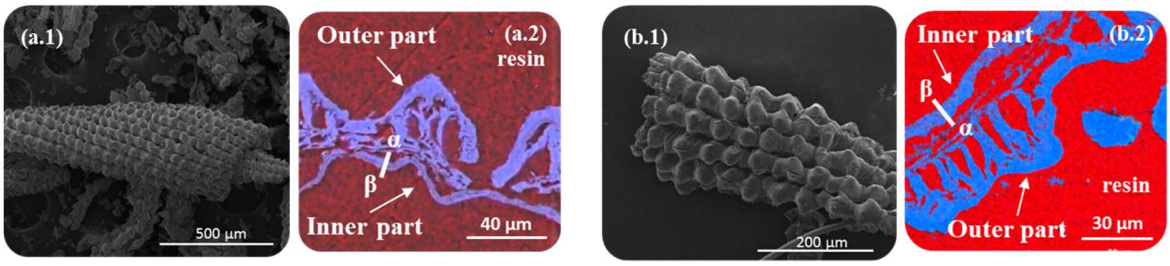

Figure 3. SEM images of rice husk ash: RRHA-Air (a.1); TRHA-Air (b.1).
EDX cross section images of rice husk ash RRHA-Air (a.2); TRHA-Air (b.2) (Carbon in red and silicium/oxygen in blue).

In order to determine the impact of the acid pre-treatment on the porous texture, nitrogen adsorption-desorption isotherms were established and are presented in Figure 4.

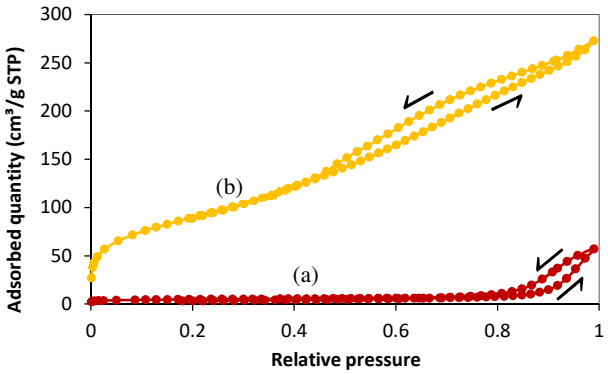

Figure 4. Nitrogen adsorption-desorption isotherms for RRHA-Air (a); TRHA-Air (b).

The TRHA-Air isotherm shows a high nitrogen adsorption capacity with a very gradual increase in the amount of nitrogen adsorbed with the equilibrium relative pressure and a wide range of mesoporosity. According to the IUPAC classification, this isotherm could be type II with a broad inflection at very low relative pressures and a steep slope at higher relative pressures, which is typical of a multimolecular adsorption on a macroporous or non-porous material. However, the non-rigid structure suggested by this type of isotherm type is inconsistent with the siliceous nature of the sample. Therefore, the isotherm must be considered as type IV which involves a mesoporous material where capillary condensation takes place. The hysteresis loop could be assimilated to a type H_1 loop without saturation plateau but with an isolated point. The RRHA-Air isotherm could also be considered as a type IV with an H_1 hysteresis loop. The

specific surface area given by the BET calculation method is 330 $m^2.g^{-1}$ for TRHA-Air and 15 $m^2.g^{-1}$ for RRHA-Air. These values are consistent with those found in the literature, although the TRHA-Air value seems to be especially high[7,54]. This difference between TRHA-Air and RRHA-Air is tremendous and needs to be explained. TEM images are presented in Figure 5 to further investigate the morphology of the samples obtained under oxidative conditions. α and β symbols describe the orientation of the thin foil (Figure 3).

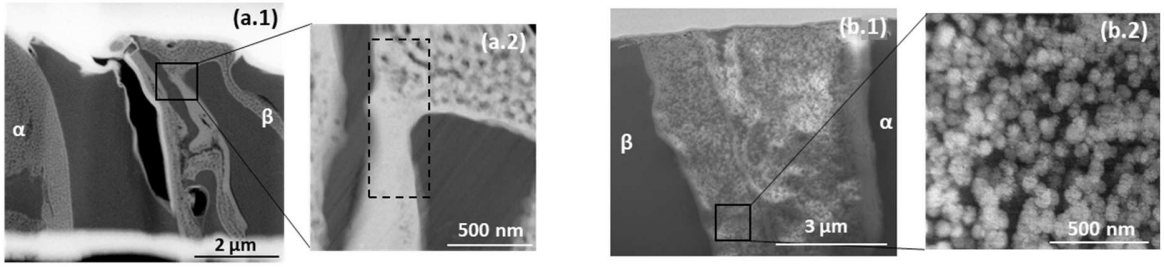

Figure 5. SEM images of a slice of rice husk ash: RRHA-Air (a.1); TRHA-Air (b.1).
TEM images of rice husk ash: RRHA-Air (a.2); TRHA-Air (b.2)

It is clear that the silica nanoparticles, which were already present in RH, are still there for TRHA-Air but seem to have been transformed for RRHA-Air. The reason why RRHA-Air has fewer nanoparticles than TRHA-Air is related to the presence of impurities. Indeed, for RRHA-Air where impurities are retained, the melting point of silica is lowered[55] which leads to the sintering of the nanoparticles. This observation is also confirmed by SAXS and SANS analyses (S.I. 4 & 5) in the high q range region where a rough interface is observed for TRHA-Air but a smooth one for RRHA-Air, which is coherent with a dense silica. This is consistent with a low specific surface area, while the morphology of the nanoparticles in the case of TRHA-Air explains the high value of the specific surface area. The particles size is 83 ± 12 nm which is in line with other authors[43], but it should be noted that many values are reported in the literature[38,39]. However, another observation on TRHA-Air can be made by looking at the outer part. At a higher magnification than the images in Figure 5, the absence of silica nanoparticles is revealed, which means that the silica is dense at this location (S.I. 6). This last observation means that two distinct silica phases coexist in the same material. To our knowledge, this observation has never been made before and authors usually consider only one of these phases.

3.3. Biochars obtained under inert atmosphere: RRHA-Ar and TRHA-Ar

The pyrolysis process results in materials with a significant carbon content in the structure and leads to the formation of biochar. As for combustion under air, the overall morphology is preserved with bumps and organisation through the silica skeleton. In the SEM and EDX images (Figure 6), it can be seen that the carbon-silica distribution is the same for both RRHA-Ar and TRHA-Ar, and corresponds to that of RRH, with silica on both sides and carbon between the silica layers. However, the carbon part seems to be aerated. The white bar in the cross section is corresponding to the location of the thin foil prepared by FIB and analysed by TEM, α and β symbols describe the orientation of the resulting sample (Figure 10).

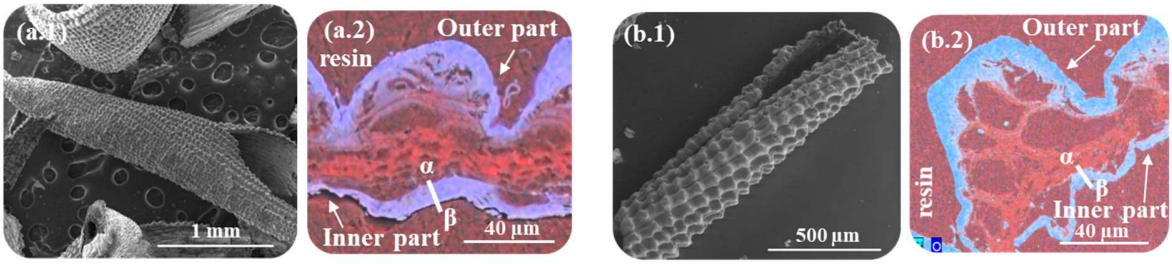

Figure 6. SEM images of rice husk biochars: RRHA-Ar (a.1); TRHA-Ar (b.1)
EDX cross section images of rice husk ash: RRHA-Ar (a.2); TRHA-Ar (b.2) (Carbon in red and silicium/oxygen in blue).

The amount of carbon is determined by TGA under air so that all remaining carbon is removed (Figure 7). This analysis shows that the RRHA-Ar degradation starts at 350 °C and ends at 470 °C with a weight loss of 32 wt%. This temperature is consistent with observations made by other authors on rice husk biochar[45]. In the case of TRHA-Ar, the degradation starts at 450 °C and ends at 650 °C with a weight loss of 50 wt%. While the proportion of carbon depends on the heat treatment and can be modified by varying the amount of oxygen in the gas mixture, the degradation temperature is solely related to the stability of the carbon. This shift may be due to an enhanced stability of the carbon phase of TRHA-Ar compared to RRHA-Ar. This enhancement may be related to the modification of organic compounds observed in Figure 2, due to the acidic treatment. Thus, the carbon formed from TRH is more stable than that of RRH.

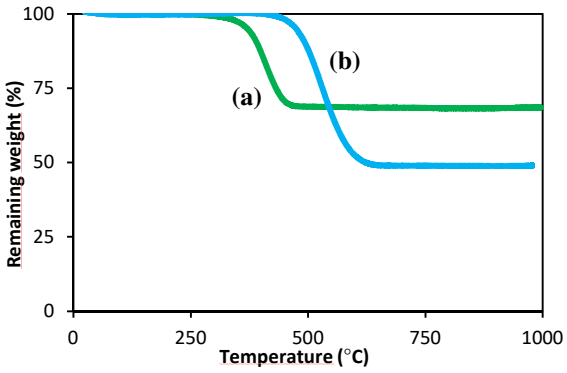

Figure 7. TGA curves for RRHA-Ar (a) and TRHA-Ar (b).

The porous textures of these two samples were analysed by N_2 adsorption-desorption and are quite similar (Figure 8).

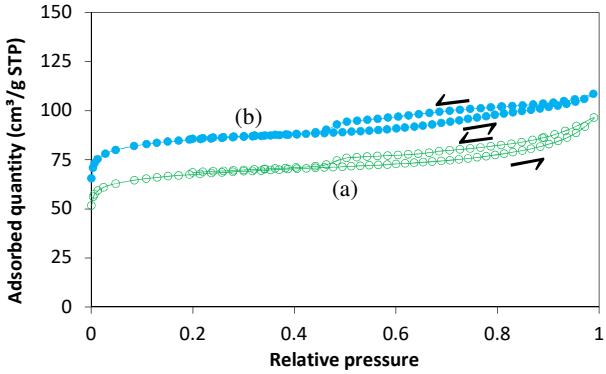

Figure 8. Nitrogen adsorption-desorption isotherms for RRHA-Ar (a); TRHA-Ar (b).

The isotherm profiles are almost identical and show an abrupt increase at very low relative pressure, indicating microporosity, and a plateau immediately after this increase despite the increase in relative pressure, meaning that there is a saturation of the sorbent. This behaviour is typical of microporous materials and is called type 1 according to the IUPAC classification. Also according to the IUPAC classification, hysteresis loops are both of type H_4. This is consistent with microporous samples having bonded sheets between which capillary condensations could occur. RRHA-Ar has a specific surface area of 260 $m^2.g^{-1}$ and TRHA-Ar 305 $m^2.g^{-1}$. Several hundred of $m^2.g^{-1}$ is a standard value for biochars[56] but seems to be quite high for a rice husk biochar[57] although some authors have already found specific surface areas of more than 200 $m^2.g^{-1}$[8,58]. The t-plot method was used. In both cases, microporosity is responsible for more than 90 % of the total specific surface area. In the study of the ash obtained under air atmosphere, no microporosity was observed. It can be assumed that only carbon induces microporosity, as is

often observed in the case of biochars[59]. This means that most of the surface is provided by the carbonaceous part of materials. Moreover, as the surface of TRHA-Ar is lower than that of TRHA-Air, it can be considered that carbon prevents the accessibility of nitrogen to the silica in this case.

In order to find out more about the carbon nature, XRD, FTIR-ATR and NMR analyses were performed. The XRD measurement of TRHA-Ar shows a strong broad peak centered at $2\theta = 22.5\ °$ and a weak broad peak centered at $2\theta = 44.4\ °$. While the former is difficult to attribute due to the possible superposition of amorphous silica and graphite-like carbon signals[60], the latter can be assigned to the carbon phase[61]. The XRD pattern of RRHA-Ar shows the same two peaks, the first one is slightly shifted to $2\theta = 22.2\ °$ and the second one is exactly at the same position as for TRHA-Ar, at $2\theta = 44.4\ °$. The allocation of the peaks is the same as before, meaning that the overall structure of the two samples is comparable. A recurring structure observed for bio-based carbon materials is the turbostratic structure, which is similar to that of graphite with a disorganisation of the graphene sheets[62]. This structure is notably found in activated carbon[63]. The XRD pattern in Figure 9 also shows several others signals, which will be discussed later in this paper.

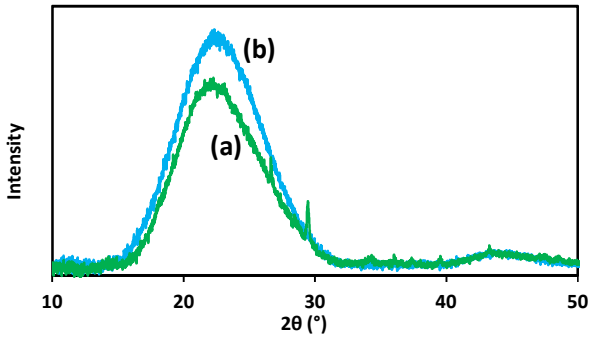

Figure 9. XRD pattern of RRHA-Ar (a) and TRHA-Ar (b).

The ^{13}C NMR and FTIR-ATR analyses are consistent with the turbsotratic structure of the carbon with the presence of typical aromatic ring signals[64] (S.I. 7). The FTIR-ATR spectra also indicate that the silica and carbon are not chemically bound but only physically mixed in two distinct phases[65,66] (S.I. 8). This is confirmed by TEM observations (Figure 10). α and β symbols describe the orientation of the thin foil (Figure 6).

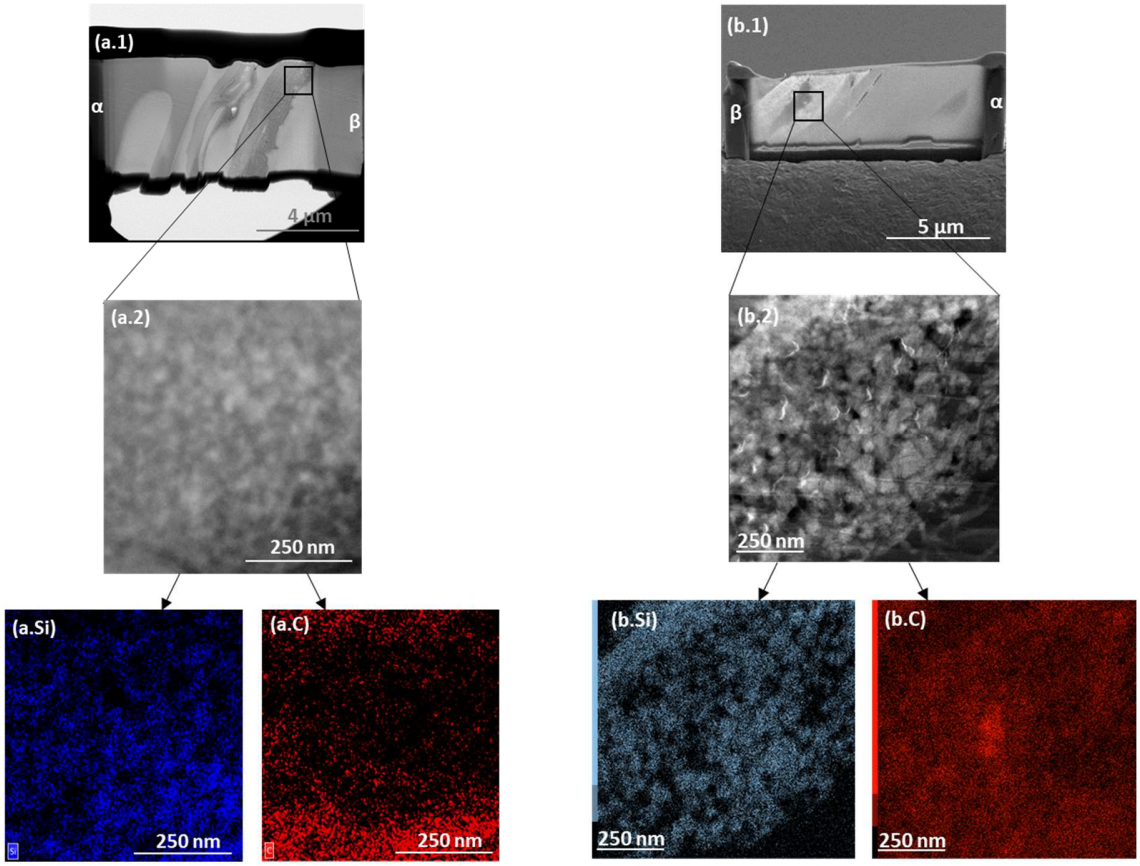

Figure 10. SEM images of a slice of rice husk biochars: RRHA-Ar (a.1); TRHA-Ar (b.1).
TEM images of rice husk ash and associated EDX: RRHA-Ar (a.2); TRHA-Ar (b.2) (Silicium in blue and carbon in red)

These images show that the silica nanoparticles are still present but embedded in a carbonaceous gangue. The measured size of nanoparticles is 30-35 nm for TRHA-Ar and 50-55 nm for RRHA-Ar. This difference in size could be explained by the sintering effect that occurs in the case of RRHA-Ar due to the presence of impurities as in the case of RRHA-Air, leading to larger particles. However, the carbonaceous part between these nanoparticles seems to limit the sintering phenomena to those that are already in contact. To confirm this, RRHA-Ar was calcined at low temperature (< 500 °C) under air atmosphere to remove the carbon. The resulting siliceous material, called RRHA-Ar-ØC, presents a specific surface area of 85 $m^2.g^{-1}$, which is more than 5 times that of RRHA-Air (S.I. 9) and thus confirms that sintering was prevented by the presence of carbon. This observation has never been made in the literature.

3.4. Characterisation of the impurities

Several mineral impurities were previously identified in this paper for RRH ash such as K, Ca, Mn or Al. In order to characterise the exact composition of these impurities for RRHA-Air and RRHA-Ar, the XRD patterns were studied in more details (Figure 11) and XPS analysis were also performed (S.I. 10 & 11). Firstly, the XRD patterns reveal the presence of cristobalite (22 and 36 °) and quartz (26.6 °). While the cristobalite is formed during the heat treatment of RH[67-70], the quartz is more likely due to the presence of sand from the production site due to the lack of washing treatment after RH collecting stage. The analysis of the other peaks shows the presence of various compounds such as KCl, $CaCO_3$ or Al_2O_3. Some of these compounds have already been observed on rice husk[45] or on other biochars[5,71]. The XPS analyses of Si, O, K and Ca also provide information on the nature of these compounds. The decomposition of the signal makes it possible to identify the bonds involved and finally the corresponding compounds.

To achieve a coherent decomposition of the spectra, a large number of strict rules have to be taken into account to assign each signal to a specific contribution (S.I. 12). These contributions could be assimilated to those of K_2O, KCl and $CaCO_3$ for impurities, Q^4 Si and Q^3 Si with bridging (BO) and non-bridging oxygen (NBO). The presence of Q^4 Si and Q^3 Si is also revealed by NMR analysis (S.I. 13) and the presence of NBO is confirmed by FTIR-ATR analysis, as well as the presence of cristobalite (S.I. 14). The ash is obtained by heat treatment and therefore very few surface hydroxyl are expected. This means that the NBO are probably induced by the presence of charge compensators such as K or Ca in the silica lattice.

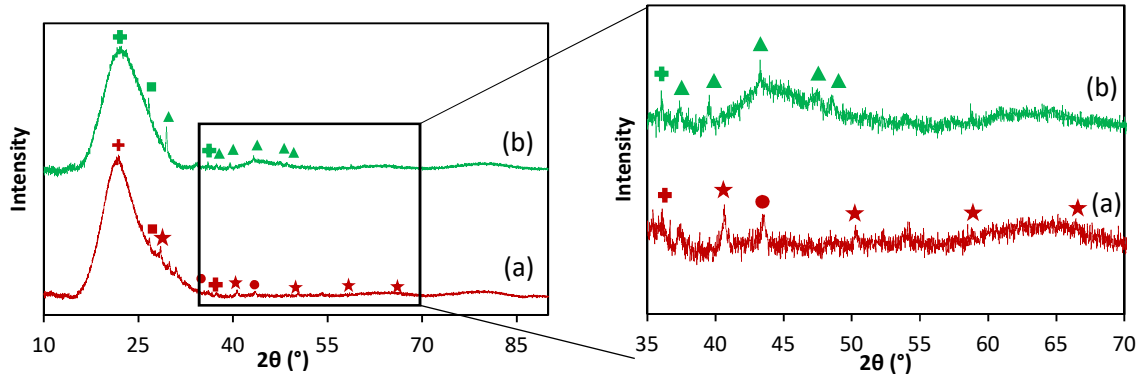

Figure 11. XRD pattern of RRHA-Air (a) and RRHA-Ar (b).
(✚ : Cristobalite[72] ; ■ : Quartz[73] ; ★ : KCl[74] ; ▲ : $CaCO_3$[75] ; ● : Al_2O_3[76])

In order to reveal more inorganic compounds and to understand where they are located in the husk, SEM-EDX observations were made (Figure 12). These images show an enveloped

RRHA-Air particle. The revealed surface is just beneath some missing outer bumps. It can be seen that the elements are present in the husk locally and form compounds with several atoms such as Ca+S, K+S, K+Cl or Mg+P. These compounds cannot be identified by SEM-EDX alone because each salt can be present in different forms (sulphate, sulphite, phosphate, phosphite, hydrate, hydrogenate, etc.) until they are characterised by XRD. Furthermore, SEM analyses of other samples revealed that the nature of the salts can vary but always appears as a bright spot on the image. Thus, Ca+P, K+P or Mg+S can also be observed. This highlights the wide variety of mineral impurities present on rice husk ash. The presence of bright spots means that some impurities are present as a separate inclusion on the husk and are actually differentiated from it. The calcium particles, which could be calcium carbonate according to the XRD pattern shown in Figure 11, exhibit a diameter ranging between 3.5 and 4.5 µm.

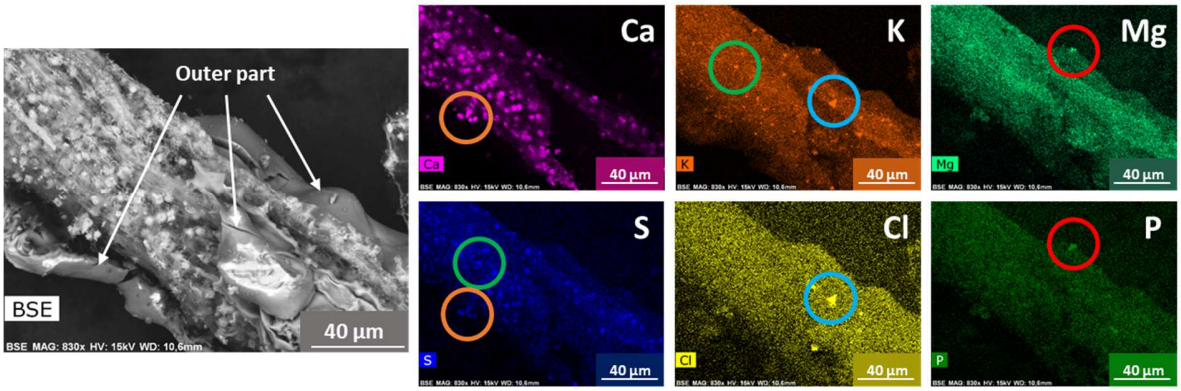

Figure 12. SEM-EDX images of RRHA-Air.

In addition, TEM-EDX images (Figure 13) showed that mineral impurities are evenly distributed in the material. These images were obtained from the thin foil reported in Figure 5.a.

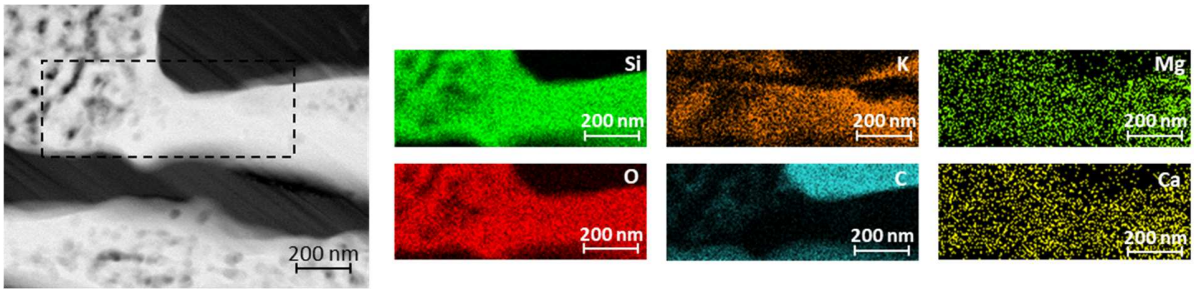

Figure 13. TEM-EDX images of RRHA-Air.

These two observations confirm that mineral impurities are present in the ash as local inclusions and in the silica lattice.

The most important information to be drawn from this third section are shown in Table 1.

Table 1. Principal information about all materials.

Sample reference	Impurities	Specific surface area	Silica type	Carbon type
TRHA-Air	No	330	Amorphous	/
TRHA-Ar	No	305	Amorphous	Turbostratic
RRHA-Air	Yes	15	Amorphous/Cristobalite	/
RRHA-Ar	Yes	260	Amorphous/Cristobalite	Turbostratic

3.5. Preliminary extraction test

The intended application for the materials obtained from rice husks is extraction of metallic elements and/or organic compounds from aqueous solutions. For this reason, extraction tests with nickel were carried out to compare all materials. The results show that RRHAs are much more efficient than TRHAs, with an extraction rate of more than 98.8 % for RRHAs while it is only 3 % for TRHAs as shows in Figure 14. These results underline that the extraction mechanisms are not driven by the available specific surface area due to the small amount of surface area in the case of RRHA-Air. The main difference between these materials that could explain the extraction efficiency is the presence or absence of impurities. Such an observation has already been made for other biochars[71,77,78] but not for rice husk ash, even though some authors have proven the usefulness of certain mineral compounds in rice husk ash, especially phosphates[9,16,23]. For this reason, a mechanism in which impurities are the main driver of extraction is suggested as in the case of several biochars[71,79]. Extraction mechanisms and the interactions between metals and RRHA will be studied and discussed in details in a future article.

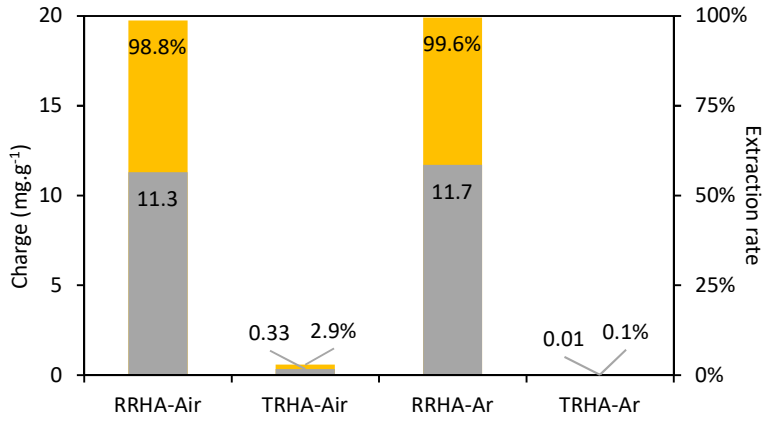

Figure 14. Extraction rate for Ni^{2+} with all materials.

In this section, several observations have been made for the first time on rice husk and its derivatives. Firstly, silica can be present in rice husk ash in several forms, namely nanoparticles and dense, and these forms can be present simultaneously. Secondly, turbostratic carbon is present between the silica nanoparticles and can limit the sintering of the silica, leading to a higher specific surface area if removed after thermal conversion. Finally, mineral impurities are present in various forms and are crucial for the removal of metals from wastewater.

4. Conclusion

This study shows that silica has a specific nanostructure in the rice husk. Silica has two distinct structures, a dense part and a divided part composed of nanoparticles. These structures are inherent in the raw husk and can only be retained after heat treatment if the impurities are removed. Indeed, if mineral impurities are retained, they accelerate the sintering and crystallisation process of the silica nanoparticles and thus reduce the specific surface area delivered by the material from 330 $m^2.g^{-1}$ for TRHA-Air to only 15 $m^2.g^{-1}$ for RRHA-Air. However, by retaining a carbonaceous portion of the husk through a pyrolysis process, the turbostratic carbon present between the silica nanoparticles prevents their sintering and allows them to be preserved. The carbon also provides a microporosity which represents 90 % of the total available porosity. The specific surface area shows little difference between raw and treated rice husk biochars and is around 300 $m^2.g^{-1}$. Finally, the nature and distribution of mineral impurities were examined. They are composed of K, Ca, Al and Mg among others, complexed with S, P or Cl to form different salts. Some compounds can be formally identified by XRD and

XPS, such as KCl or $CaCO_3$. These mineral salts are located along the surface of the husk as individual aggregates but are also present in the silica lattice as charge compensators. One of the crucial information presented in this paper is that these impurities are essential for the removal of heavy metal pollutants such as nickel. Indeed, the extraction rate of RRHA-Air is almost 99 % with a capacity of 11.3 $mg.g^{-1}$ and the extraction rate of RRHA-Ar is over 99.5 % with a capacity of 11.7 $mg.g^{-1}$. The extraction rates of TRHA materials are less than 3 % with a capacity of less than 0.5 $mg.g^{-1}$. The mechanism involved in metal extraction will be discussed in depth in another article, but it can already be conclude that RH is a promising material for the development of a wastewater treatment materials.

Author information

The manuscript was written through contributions of all authors. All authors have given approval to the final version of the manuscript. The authors declare no conflict of interest.

Acknowledgment

We would like to thank all people with whom we worked, especially Martiane CABIE (Marseille University, France) for the FIB preparation, Davy CAROLE (Lyon University, France) for the fused bead preparation, Ovidiu ERSEN and Walid BAAZIZ (Strasbourg University, France) for the TEM images, Valérie FLAUD (Institut Charles Gerhardt, ICGM, UMR 5253, Montpellier University, France) for the XPS analyses, Jacques JESTIN (Léon Brillouin Laboratory, CEA, France) for the SANS analyses, Sandra MAYNADIE (ICSM, France) for the NMR analyses and Olivier TACHE (CEA Saclay, France) for the USAXS analyses. The authors acknowledge financial support from the CNRS-CEA “METSA” French network (FR CNRS 3507) (METSA, 2018) for the TEM experiments conducted at the Institut de Physique et de Chimie des Matériaux de Strasbourg platform (IPCMS, UMR 7504, Strasbourg, France). The authors also acknowledge gracious support of the Silos de Tourtoulen for the furniture of rice husk.

Appendix

Supplementary information

References

1. Zinatloo-Ajabshir, S.; Mortazavi-Derazkola, S.; Salavati-Niasari, M., Nd2O3-SiO2 nanocomposites: A simple sonochemical preparation, characterization and photocatalytic activity. *Ultrasonics Sonochemistry* **2018**, 42, 171-182. DOI: https://doi.org/10.1016/j.ultsonch.2017.11.026

2. Zinatloo-Ajabshir, S.; Morassaei, M.S.; Salavati-Niasari, M., Eco-friendly synthesis of Nd2Sn2O7–based nanostructure materials using grape juice as green fuel as photocatalyst for the degradation of erythrosine. *Composites Part B: Engineering* **2019**, 167, 643-653. DOI: https://doi.org/10.1016/j.compositesb.2019.03.045

3. Etemadi, H.; Afsharkia, S.; Zinatloo-Ajabshir, S.; Shokri, E., Effect of alumina nanoparticles on the antifouling properties of polycarbonate-polyurethane blend ultrafiltration membrane for water treatment. *Polymer Engineering & Science* **2021**, 61 (9), 2364-2375. DOI: https://doi.org/10.1002/pen.25764

4. Inyang, M.; Dickenson, E., The potential role of biochar in the removal of organic and microbial contaminants from potable and reuse water: A review. *Chemosphere* **2015**, 134, 232-240. DOI: https://doi.org/10.1016/j.chemosphere.2015.03.072

5. Inyang, M.I.; Gao, B.; Yao, Y.; Xue, Y.; Zimmerman, A.; Mosa, A.; Pullammanappallil, P.; Ok, Y.S.; Cao, X., A review of biochar as a low-cost adsorbent for aqueous heavy metal removal. *Critical Reviews in Environmental Science and Technology* **2016**, 46 (4), 406-433.

6. "Food and Agriculture Organization of the United Nations : FAOSTAT." http://www.fao.org/faostat/en/#data/QC/visualize (accessed 21/09/2021).

7. Foo, K.Y.; Hameed, B.H., Utilization of rice husk ash as novel adsorbent: A judicious recycling of the colloidal agricultural waste. *Advances in Colloid and Interface Science* **2009**, 152 (1), 39-47. DOI: https://doi.org/10.1016/j.cis.2009.09.005

8. Liou, T.-H., Evolution of chemistry and morphology during the carbonization and combustion of rice husk. *Carbon* **2004**, 42 (4), 785-794. DOI: https://doi.org/10.1016/j.carbon.2004.01.050

9. Huang, F.; Gao, L.Y.; Wu, R.R.; Wang, H.; Xiao, R.B., Qualitative and quantitative characterization of adsorption mechanisms for Cd(2+) by silicon-rich biochar. *Sci Total Environ* **2020**, 731, 139163. DOI: 10.1016/j.scitotenv.2020.139163

10. Kaur, S.; Walia, T.; Mahajan, R., Comparative studies of zinc, cadmium, lead and copper on economically viable adsorbents. *Journal of Environmental engineering and Science* **2008**, 7 (1), 83-90.

11. Srivastava, V.C.; Mall, I.D.; Mishra, I.M., Adsorption thermodynamics and isosteric heat of adsorption of toxic metal ions onto bagasse fly ash (BFA) and rice husk ash (RHA). *Chemical Engineering Journal* **2007**, 132 (1), 267-278. DOI: https://doi.org/10.1016/j.cej.2007.01.007

12. Gad, H.; Omar, H.; Aziz, M.; Hassan, M.; Khalil, M., Treatment of rice husk ash to improve adsorption capacity of cobalt from aqueous solution. *J Asian Journal of Chemistry* **2016**, 28 (2), 385.

13. Nakbanpote, W.; Goodman, B.A.; Thiravetyan, P., Copper adsorption on rice husk derived materials studied by EPR and FTIR. *Colloids and Surfaces A: Physicochemical and Engineering Aspects* **2007**, 304 (1), 7-13. DOI: https://doi.org/10.1016/j.colsurfa.2007.04.013

14. Naeem, S.; Zahra, N.; Zafar, U., Adsorption Studies of Copper on Rice Husk Ash (RHA). *Bangladesh Journal of Scientific and Industrial Research* **2011**, 45 (4), 367-370. DOI: 10.3329/bjsir.v45i4.7382

15. Vieira, M.G.A.; Almeida Neto, A.F.d.; Silva, M.G.C.d.; Carneiro, C.N.; Melo Filho, A.A., Adsorption of lead and copper ions from aqueous effluents on rice husk ash in a dynamic system. *Brazilian Journal of Chemical Engineering* **2014**, 31, 519-529.

16. Aran, D.; Antelo, J.; Fiol, S.; Macias, F., Influence of feedstock on the copper removal capacity of waste-derived biochars. *Bioresour Technol* **2016**, 212, 199-206. DOI: 10.1016/j.biortech.2016.04.043

17. Tiwari, D.; Singh, D.; Saksena, D., Hg (II) adsorption from aqueous solutions using rice-husk ash. *Journal of Environmental Engineering* **1995**, 121 (6), 479-481.

18. Feng, Q.; Lin, Q.; Gong, F.; Sugita, S.; Shoya, M., Adsorption of lead and mercury by rice husk ash. *Journal of Colloid and Interface Science* **2004**, 278 (1), 1-8. DOI: https://doi.org/10.1016/j.jcis.2004.05.030

19. Srivastava, V.C.; Mall, I.D.; Mishra, I.M., Characterization of mesoporous rice husk ash (RHA) and adsorption kinetics of metal ions from aqueous solution onto RHA. *Journal of Hazardous Materials* **2006**, 134 (1), 257-267. DOI: https://doi.org/10.1016/j.jhazmat.2005.11.052

20. Shen, Z.; Zhang, Y.; McMillan, O.; Jin, F.; Al-Tabbaa, A., Characteristics and mechanisms of nickel adsorption on biochars produced from wheat straw pellets and rice husk. *Environ Sci Pollut Res Int* **2017**, 24 (14), 12809-12819. DOI: 10.1007/s11356-017-8847-2

21. Wang, L.-H.; Lin, C.-I., Adsorption of Lead(II) Ion from Aqueous Solution Using Rice Hull Ash. *Industrial & Engineering Chemistry Research* **2008**, 47 (14), 4891-4897. DOI: 10.1021/ie071521z

22. Naiya, T.K.; Bhattacharya, A.K.; Mandal, S.; Das, S.K., The sorption of lead(II) ions on rice husk ash. *Journal of Hazardous Materials* **2009**, 163 (2), 1254-1264. DOI: https://doi.org/10.1016/j.jhazmat.2008.07.119

23. Xu, X.; Cao, X.; Zhao, L., Comparison of rice husk- and dairy manure-derived biochars for simultaneously removing heavy metals from aqueous solutions: role of mineral components in biochars. *Chemosphere* **2013**, 92 (8), 955-961. DOI: 10.1016/j.chemosphere.2013.03.009

24. Shi, J.; Fan, X.; Tsang, D.C.W.; Wang, F.; Shen, Z.; Hou, D.; Alessi, D.S., Removal of lead by rice husk biochars produced at different temperatures and implications for their environmental utilizations. *Chemosphere* **2019**, 235, 825-831. DOI: 10.1016/j.chemosphere.2019.06.237

25. Bhattacharya, A.; Mandal, S.; Das, S., Adsorption of Zn (II) from aqueous solution by using different adsorbents. *Chemical Engineering Journal* **2006**, 123 (1-2), 43-51.

26. El-Said, A.; Badawy, N.; Garamon, S., Adsorption of Heavy Metal Ions from Aqueous Solutions onto Rice Husk Ash Low Cost Adsorbent. *Journal of Environmental & Analytical Toxicology* **2018**, 8 (1). DOI: 10.4172/2161-0525.1000543

27. Chou, K.-S.; Tsai, J.-C.; Lo, C.-T., The adsorption of Congo red and vacuum pump oil by rice hull ash. *Bioresource Technology* **2001**, 78 (2), 217-219.

28. Chandrasekhar, S.; Pramada, P., Rice husk ash as an adsorbent for methylene blue—effect of ashing temperature. *Adsorption* **2006**, 12 (1), 27.

29. Lakshmi, U.R.; Srivastava, V.C.; Mall, I.D.; Lataye, D.H., Rice husk ash as an effective adsorbent: Evaluation of adsorptive characteristics for Indigo Carmine dye. *Journal of Environmental Management* **2009**, 90 (2), 710-720. DOI: https://doi.org/10.1016/j.jenvman.2008.01.002

30. Lataye, D.H.; Mishra, I.M.; Mall, I.D., Pyridine sorption from aqueous solution by rice husk ash (RHA) and granular activated carbon (GAC): Parametric, kinetic, equilibrium and thermodynamic aspects. *Journal of Hazardous Materials* **2008**, 154 (1), 858-870. DOI: https://doi.org/10.1016/j.jhazmat.2007.10.111

31. Mbui, D.N.; Shiundu, P.M.; Ndonye, R.M.; Kamau, G.N., Adsorption and detection of some phenolic compounds by rice husk ash of Kenyan origin. *Journal of Environmental Monitoring* **2002**, 4 (6), 978-984.

32. Mahvi, A.; Maleki, A.; Eslami, A., Potential of rice husk and rice husk ash for phenol removal in aqueous systems. *American Journal of Applied Sciences* **2004**, 1 (4), 321-326.

33. Kermani, M.; Pourmoghaddas, H.; Bina, B.; Khazaei, Z., Removal of phenol from aqueous solutions by rice husk ash and activated carbon. *Pak J Biol Sci* **2006**, 9 (10), 1905-1910.

34. Amran, M.; Fediuk, R.; Murali, G.; Vatin, N.; Karelina, M.; Ozbakkaloglu, T.; Krishna, R.S.; Sahoo, A.K.; Das, S.K.; Mishra, J., Rice Husk Ash-Based Concrete Composites: A Critical Review of Their Properties and Applications. *Crystals* **2021**, 11 (2), 168. DOI: 10.3390/cryst11020168

35. Singh, B. Rice husk ash. In *Waste and supplementary cementitious materials in concrete*; Elsevier, **2018**; pp 417-460.

36. Chandrasekhar, S.; Pramada, P.N.; Praveen, L., Effect of organic acid treatment on the properties of rice husk silica. *Journal of Materials Science* **2005**, 40 (24), 6535-6544. DOI: 10.1007/s10853-005-1816-z

37. Vishwakarma, V.; Ramachandran, D.; Anbarasan, N.; Rabel, A.M., Studies of rice husk ash nanoparticles on the mechanical and microstructural properties of the concrete. *J Materials Today: Proceedings* **2016**, 3 (6), 1999-2007.

38. Wang, W.; Martin, J.C.; Fan, X.; Han, A.; Luo, Z.; Sun, L., Silica nanoparticles and frameworks from rice husk biomass. *J ACS applied materials interfaces* **2012**, 4 (2), 977-981.

39. Wang, Z.; Smith, A.T.; Wang, W.; Sun, L., Versatile Nanostructures from Rice Husk Biomass for Energy Applications. *Angew. Chem. Int. Ed.* **2018**, 57 (42), 13722-13734. DOI: https://doi.org/10.1002/anie.201802050

40. Shen, Y., Rice husk silica derived nanomaterials for sustainable applications. *Renewable and Sustainable Energy Reviews* **2017**, 80, 453-466. DOI: https://doi.org/10.1016/j.rser.2017.05.115

41. Tabata, S.; Iida, H.; Horie, T.; Yamada, S., Hierarchical porous carbon from cell assemblies of rice husk for in vivo applications. *J MedChemComm* **2010**, 1 (2), 136-138.

42. Muroya, M.; Kondo, S., The effect of impurities upon the physical properties of silica gel by the heat-treatment. *J Bulletin of the Chemical Society of Japan* **1970**, 43 (11), 3453-3456.

43. Liu, N.; Huo, K.; McDowell, M.T.; Zhao, J.; Cui, Y., Rice husks as a sustainable source of nanostructured silicon for high performance Li-ion battery anodes. *Sci Rep* **2013**, 3, 1919. DOI: 10.1038/srep01919

44. Liu, D.; Zhang, W.; Lin, H.; Li, Y.; Lu, H.; Wang, Y., Hierarchical porous carbon based on the self-templating structure of rice husk for high-performance supercapacitors. *J RSC advances* **2015**, 5 (25), 19294-19300.

45. Prakongkep, N.; Gilkes, R.J.; Wiriyakitnateekul, W.; Duangchan, A.; Darunsontaya, T., The effects of pyrolysis conditions on the chemical and physical properties of rice husk biochar. *J Int. J. Mater. Sci* **2013**, 3 (3), 97-103.

46. Dizaji, H.B.; Zeng, T.; Hölzig, H.; Bauer, J.; Klöß, G.; Enke, D., Ash transformation mechanism during combustion of rice husk and rice straw. *J Fuel* **2022**, 307, 121768.

47. Willis, J. Glass beads by borate fusion. In *Understanding XRF spectrometry*, Vol. 2; PANalytical, **2010**.

48. Jung, D.S.; Ryou, M.-H.; Sung, Y.J.; Park, S.B.; Choi, J.W., Recycling rice husks for high-capacity lithium battery anodes. *Proceedings of the National Academy of Sciences* **2013**, 110 (30), 12229-12234. DOI: doi:10.1073/pnas.1305025110

49. Mansaray, K.G.; Ghaly, A.E., Thermogravimetric Analysis of Rice Husks in an Air Atmosphere. *Energy Sources* **1998**, 20 (7), 653-663. DOI: 10.1080/00908319808970084

50. Yin, C.-Y.; Goh, B.-M., Thermal degradation of rice husks in air and nitrogen: thermogravimetric and kinetic analyses. *J Energy Sources, Part A: Recovery, Utilization, Environmental Effects* **2011**, 34 (3), 246-252.

51. Genieva, S.D.; Turmanova, S.C.; Dimitrova, A.S.; Vlaev, L.T., Characterization of rice husks and the products of its thermal degradation in air or nitrogen atmosphere. *Journal of Thermal Analysis and Calorimetry* **2008**, 93 (2), 387. DOI: 10.1007/s10973-007-8429-5

52. Alhinai, M.; Azad, A.K.; Bakar, M.S.A.; Phusunti, N., Characterisation and thermochemical conversion of rice husk for biochar production. *J Int. J. Renew. Energy Res* **2018**, 8 (3), 1648-1656.

53. Javed, M.A., Acid treatment effecting the physiochemical structure and thermal degradation of biomass. *Renewable Energy* **2020**, 159, 444-450. DOI: https://doi.org/10.1016/j.renene.2020.06.011

54. Bakar, R.A.; Yahya, R.; Gan, S.N., Production of High Purity Amorphous Silica from Rice Husk. *Procedia Chemistry* **2016**, 19, 189-195. DOI: 10.1016/j.proche.2016.03.092

55. Umeda, J.; Kondoh, K., High-purification of amorphous silica originated from rice husks by combination of polysaccharide hydrolysis and metallic impurities removal. *Industrial Crops and Products* **2010**, 32 (3), 539-544. DOI: https://doi.org/10.1016/j.indcrop.2010.07.002

56. Weber, K.; Quicker, P., Properties of biochar. *Fuel* **2018**, 217, 240-261. DOI: 10.1016/j.fuel.2017.12.054

57. Asadi, H.; Ghorbani, M.; Rezaei-Rashti, M.; Abrishamkesh, S.; Amirahmadi, E.; Chengrong, C.; Gorji, M., Application of Rice Husk Biochar for Achieving Sustainable Agriculture and Environment. *Rice Science* **2021**, 28 (4), 325-343. DOI: 10.1016/j.rsci.2021.05.004

58. Rostamian, R.; Heidarpour, M.; Mousavi, S.; Afyuni, M., Characterization and Sodium Sorption Capacity of Biochar and Activated Carbon Prepared from Rice Husk. *J. Agr. Sci. Tech.* **2015**, 17, 1057-1069.

59. Jimenez-Cordero, D.; Heras, F.; Alonso-Morales, N.; Gilarranz, M.A.; Rodriguez, J.J., Porous structure and morphology of granular chars from flash and conventional pyrolysis of grape seeds. *Biomass and Bioenergy* **2013**, 54, 123-132. DOI: https://doi.org/10.1016/j.biombioe.2013.03.020

60. Larichev, Y.V.; Yeletsky, P.M.; Yakovlev, V.A., Study of silica templates in the rice husk and the carbon–silica nanocomposites produced from rice husk. *Journal of Physics and Chemistry of Solids* **2015**, 87, 58-63. DOI: https://doi.org/10.1016/j.jpcs.2015.07.025

61. Sazali, N.E.S.; Deraman, M.; Omar, R.; Othman, M.A.R.; Suleman, M.; Shamsudin, S.A.; Tajuddin, N.S.M.; Hanappi, M.F.Y.M.; Hamdan, E.; Nor, N.S.M.; Basri, N.H., Preparation and

structural characterization of turbostratic-carbon/graphene derived from amylose film. *In AIP Conference Proceedings* **2016**, 1784 (1), 040009. DOI: 10.1063/1.4966795

62. Marsh, H.; Griffiths, J., New Processes and New Applications. *Ext. Abst. of International Symposium on Carbon, Toyohashi, Japan* **1982**, 81.

63. Qu, D., Studies of the activated carbons used in double-layer supercapacitors. *Journal of Power Sources* **2002**, 109 (2), 403-411. DOI: https://doi.org/10.1016/S0378-7753(02)00108-8

64. McBeath, A.V.; Smernik, R.J.; Krull, E.S.; Lehmann, J., The influence of feedstock and production temperature on biochar carbon chemistry: A solid-state 13C NMR study. *Biomass and Bioenergy* **2014**, 60, 121-129. DOI: https://doi.org/10.1016/j.biombioe.2013.11.002

65. Al-Oweini, R.; El-Rassy, H., Synthesis and characterization by FTIR spectroscopy of silica aerogels prepared using several Si(OR)4 and R″Si(OR′)3 precursors. *Journal of Molecular Structure* **2009**, 919 (1), 140-145. DOI: https://doi.org/10.1016/j.molstruc.2008.08.025

66. Keiluweit, M.; Nico, P.S.; Johnson, M.G.; Kleber, M., Dynamic Molecular Structure of Plant Biomass-Derived Black Carbon (Biochar). *Environmental Science & Technology* **2010**, 44 (4), 1247-1253. DOI: 10.1021/es9031419

67. Rozainee, M.; Ngo, S.P.; Salema, A.A.; Tan, K.G.; Ariffin, M.; Zainura, Z.N., Effect of fluidising velocity on the combustion of rice husk in a bench-scale fluidised bed combustor for the production of amorphous rice husk ash. *Bioresource Technology* **2008**, 99 (4), 703-713. DOI: https://doi.org/10.1016/j.biortech.2007.01.049

68. Patel, M.; Karera, A.; Prasanna, P., Effect of thermal and chemical treatments on carbon and silica contents in rice husk. *Journal of Materials Science* **1987**, 22 (7), 2457-2464. DOI: 10.1007/BF01082130

69. Hamad, M.A.; Khattab, I.A., Effect of the combustion process on the structure of rice hull silica. *Thermochimica Acta* **1981**, 48 (3), 343-349. DOI: https://doi.org/10.1016/0040-6031(81)80255-9

70. Della, V.P.; Kühn, I.; Hotza, D., Rice husk ash as an alternate source for active silica production. *Materials Letters* **2002**, 57 (4), 818-821. DOI: https://doi.org/10.1016/S0167-577X(02)00879-0

71. Xu, X.; Zhao, Y.; Sima, J.; Zhao, L.; Masek, O.; Cao, X., Indispensable role of biochar-inherent mineral constituents in its environmental applications: A review. *Bioresour Technol* **2017**, 241, 887-899. DOI: 10.1016/j.biortech.2017.06.023

72. "Cristobalite R060648." https://rruff.info/cristobalite/display=default/R060648 (accessed 16/01/2018).

73. "Quartz R040031." https://rruff.info/quartz/display=default/R040031 (accessed 16/01/2018).

74. "Sylvite R050166." https://rruff.info/chem=K,Cl/notchem=all/display=default/ (accessed 03/03/2020).

75. "Calcite R040070." https://rruff.info/chem=Ca,C,O/notchem=all/display=default/R040070 (accessed 03/03/2020).

76. "Corundum R040096." https://rruff.info/chem=O,Al/notchem=all/display=default/R040096 (accessed 03/03/2020).

77. Inyang, M.; Gao, B.; Ding, W.; Pullammanappallil, P.; Zimmerman, A.R.; Cao, X., Enhanced Lead Sorption by Biochar Derived from Anaerobically Digested Sugarcane Bagasse. *Separation Science and Technology* **2011**, 46 (12), 1950-1956. DOI: 10.1080/01496395.2011.584604

78. Wang, Z.; Liu, G.; Zheng, H.; Li, F.; Ngo, H.H.; Guo, W.; Liu, C.; Chen, L.; Xing, B., Investigating the mechanisms of biochar's removal of lead from solution. *Bioresour Technol* **2015**, 177, 308-317. DOI: 10.1016/j.biortech.2014.11.077

79. Cao, X.; Ma, L.; Gao, B.; Harris, W., Dairy-manure derived biochar effectively sorbs lead and atrazine. *J Environmental science technology* **2009**, 43 (9), 3285-3291.